

Non-invasive single-shot imaging through scattering layers and around corners via speckle correlations

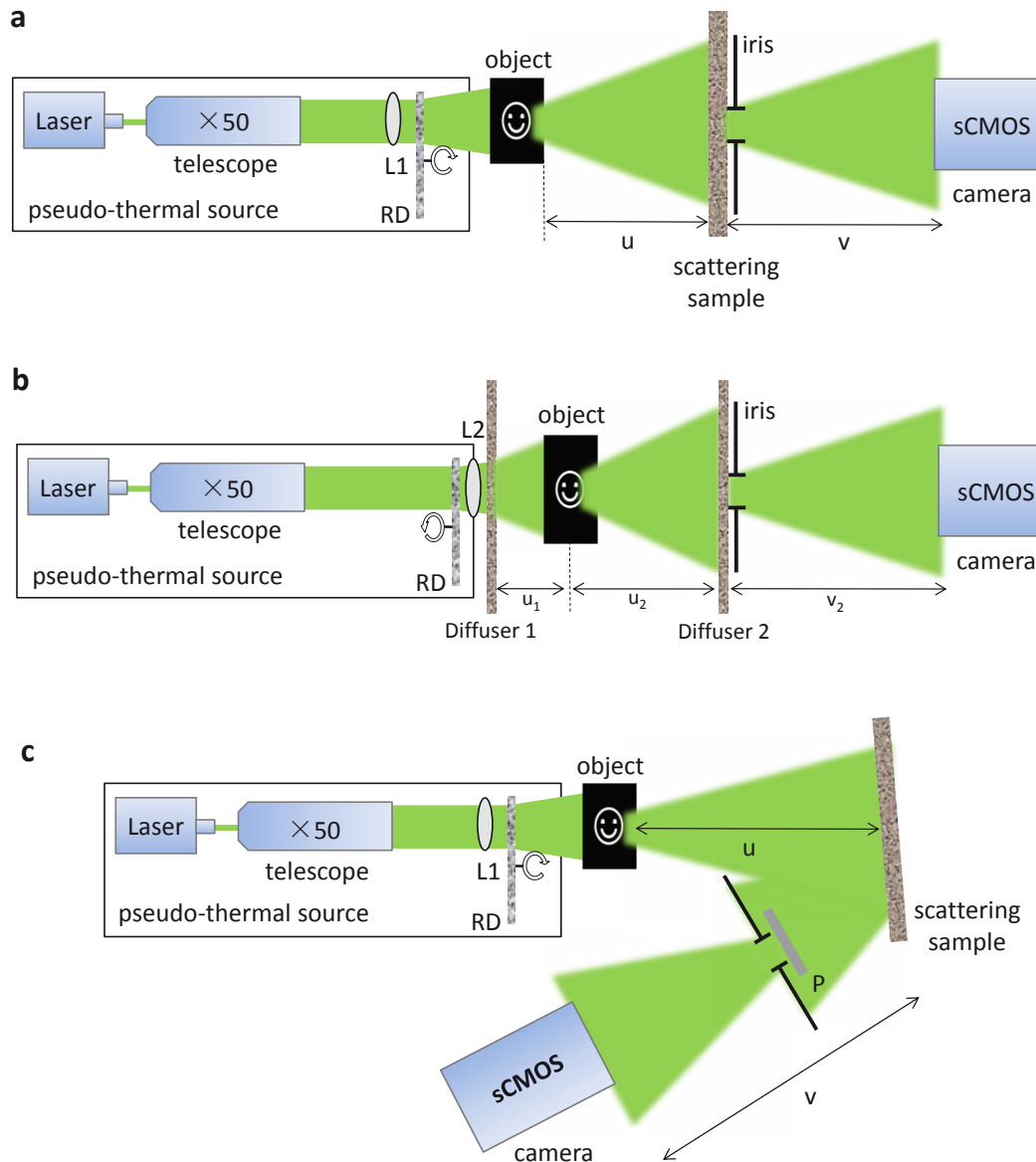
Ori Katz^{1,2}, Pierre Heidmann¹, Mathias Fink¹, Sylvain Gigan^{1,2}

¹ Institut Langevin, UMR7587 ESPCI ParisTech and CNRS, INSERM ERL U979, 1 Rue Jussieu, 75005 Paris, France

² Laboratoire Kastler Brossel, Université Pierre et Marie Curie, Ecole Normale Supérieure, CNRS, Collège de France, 24 rue Lhomond, 75005 Paris, France

1. Experimental setups

The experimental setups for imaging in transmission and in reflection are drawn schematically in Supplementary Figure 1. The light source in all the experiments was a pseudo-thermal spatially-incoherent source, composed of a Coherent Compass 215M-50 532nm CW laser, whose beam was expanded approximately $\times 50$ times by a home-built telescope and passed through a rapidly rotating diffuser. The light that passed through the object and scattered by the scattering sample was passed through a variable iris (diameter of 5mm to 10mm) before propagating to the camera. In the experiments done in reflection, a linear polarizer was placed in front of the camera to maximize the contrast of the scattered light pattern.

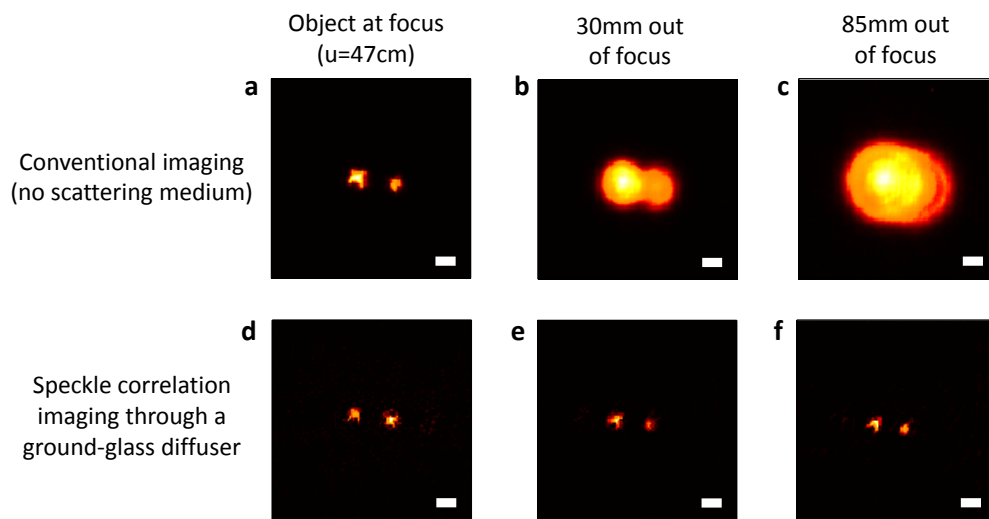


Supplementary Figure 1: Optical setups used for imaging through the scattering media (a-b) and around corners (c). RD - rotating diffuser, L1,L2 - focusing lenses ($f_{L1}=400\text{mm}/1000\text{mm}$, $f_{L2}=25\text{mm}$), P - linear polarizer. The setup in (a) was used to perform the experiments of Figs.2,5, and the setup of (b) was used for the experiment of Fig.3. Where $u_1=20\text{mm}$, $u_2=195\text{mm}$, $v_2=95\text{mm}$, diffuser 1 is a 10° light shaping diffuser (Newport), and diffuser 2 and the diffuser used in (a) is a 220 grit ground-glass diffuser (DG10-220-MD Thorlabs).

2. Experimental demonstration of the extended depth of field

In this experiment we used the setup of Supplementary Figure 1a to image a simple planar object composed of two bright spots at various distances from the scattering diffuser (DG10-220-MD Thorlabs). We compare the results to those obtained when the diffuser is replaced by a conventional single-lens imaging system having an entrance pupil of the same size. As expected, the images of the object that were obtained using our technique through the scattering medium remain sharp at all distances, whereas those taken with the conventional imaging system are sharp only when the object is near the focus of the imaging system (Supplementary Figure 2).

In our technique, similar to wavefront-coding techniques^{1,2}, the diffraction limited resolution and infinite depth of field are obtained at the price of a reduced image contrast, or equivalently at an expense of an increased dynamic range requirement from the imager (see Discussion in the main text). A downside of the extended depth of field is that in the absence of any further processing, the technique has no axial sectioning capability.



Supplementary Figure 2. Extended depth of field demonstration. Experimental comparison between the images of a two-point planar object placed at various distances, u , from the imaging setup, obtained with: **a-c**, a conventional single-lens imaging system, and **d-f**, a visually-opaque ground glass diffuser placed instead of the lens. Both systems have similar numerical apertures. Scale-bars are 10 camera pixels, corresponding to 300 μ m at the object plane of (a,d).

3. Practical limits on complexity of reconstructed objects (objects' sparsity)

In this section we analyze the practical limitations on the maximal object complexity that could be retrieved using the presented approach. The main limitation is posed by the fact that the more complex the object pattern is, i.e. the larger the number of bright resolution cells present in its image, the lower is the contrast of the measured scattered light camera image. This fact is clearly visible in the raw camera images of Figures 1-4, where the information on the object's autocorrelation is contained in a small signal modulation on top of a large background. Being able to detect this small signal on top of the large background is the main practical limit on the object's complexity. We will now analyze this requirement, and will give an estimate for the object complexity as a function of the optical and detection system parameters.

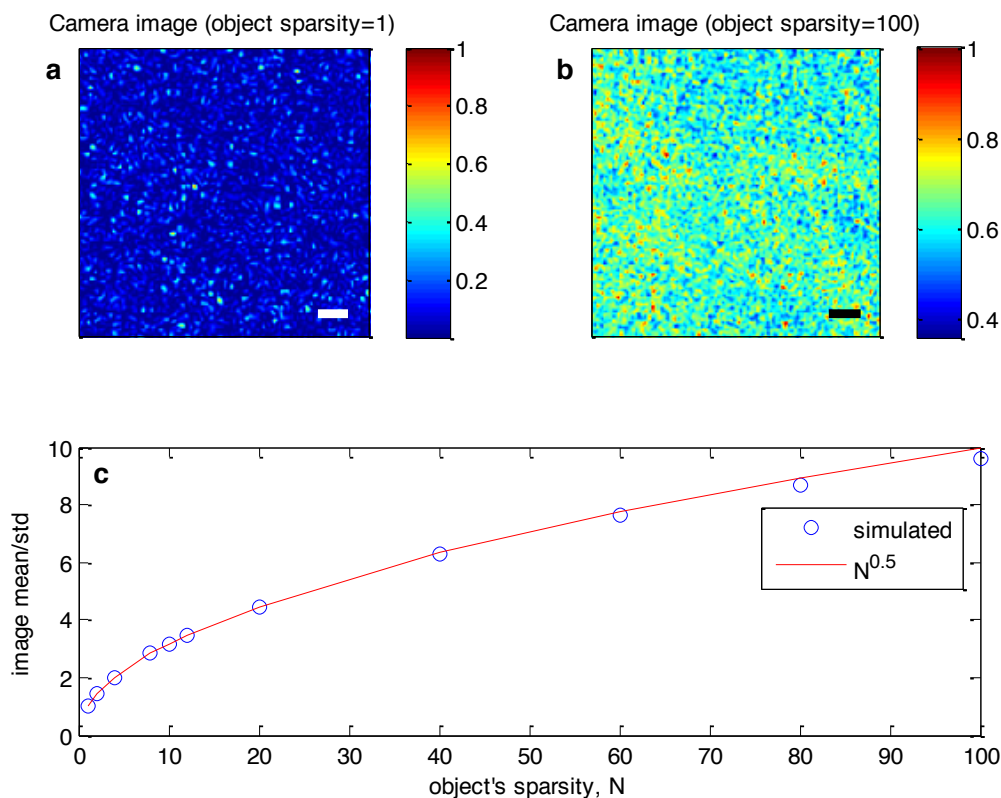
Consider an object with a complexity defined by its sparsity, N , given by the ratio between the bright area of the object to the diffraction limited resolution cell area $(u\delta\theta)^2$. The resulting camera image for this object would be composed of the intensity sum of N shifted speckle patterns (Figure 1). Because the shifted speckle patterns are uncorrelated for a shift larger than the resolution cell diameter, and as each speckle pattern has an intensity standard-deviation that is equal to its mean intensity³, *the resulting camera image would have a mean to standard deviation ratio equal to \sqrt{N}* . A numerical example of this simple result is given in Supplementary Figure 3. The technical requirement from the camera is then to be able to *detect a relative signal change of $1/\sqrt{N}$* , i.e. detect the small modulation (whose magnitude is estimated here by the image standard-deviation) on top of the large background, which is \sqrt{N} times brighter.

The most important limiting technical factor in this respect is the camera *full well capacity*, F , which defines the maximum number of electrons each camera pixel can detect before saturating. The theoretical limitation on the minimal detectable signal change at each pixel is the *shot noise* of the F detected electrons in a single shot: $\Delta N_{elec} = \sqrt{F}$. Yielding a minimal relative detectable signal change of $\Delta N_{elec}/N_{elec} = \sqrt{F}/F = 1/\sqrt{F}$. By requiring that this minimum detectable signal would be smaller than the actual signal modulation of the scattered light pattern one gets: $1/\sqrt{F} < 1/\sqrt{N}$, or simply: **$F > N$, i.e. the maximal object's sparsity, N , that can be resolved in a single shot is limited by the camera full well depth, F** . The shot-noise of the full well capacity is both the ideal limitation and also the practical limit in most modern scientific grade cameras, having sufficient bit depth. For example, the sCMOS camera used in the experiments of Figures 2-4 (PCO edge 5.5), has a full well capacity of $F=30,000e^-$, and analog-to-digital dynamic range of 16bit ($=65536$), which is much finer than the one required to resolve the shot noise fluctuations of $\sqrt{30000} \approx 173e^-$. The other relevant camera parameters, namely its readout noise and dark current are typically orders of magnitude lower (here $2.4e^-$ and $\sim 6e^-$, respectively). As a result, one can perform averaging over several camera images to increase the minimum detectable relative signal.

Of course, the number of detected photons should also be high enough to create enough electrons to fill the detector well capacity. This is dictated (and linearly dependent) by the object brightness, the camera exposure time and its quantum efficiency. In our experiments, exposure times of the order of a hundred milliseconds to two seconds were sufficient to fill the well capacity of the cameras used.

Note that:

- 1) A given object's complexity can be controlled and reduced by lowering the size of the aperture on the scattering medium where light is collected from, i.e. by sacrificing imaging resolution.
- 2) The above estimate for $F > N$ was developed assuming a required signal-to-noise ratio of 1. The actual required signal to noise ratio is dependent on the specific phase-retrieval reconstruction algorithm used, and would be simply a multiplicative factor on the required full well capacity.



Supplementary Figure 3: Raw camera image contrast as a function of the object's sparsity, N (numerical results). **a**, example for a camera image obtained for a point-like object with a sparsity of $N=1$. **b**, example for a camera image obtained for an object of sparsity $N=100$. **c**, the ratio of the camera image mean intensity to its intensity standard deviation; simulated (blue dots), and \sqrt{N} theoretical estimate. The information on the objects autocorrelation is encoded in the small intensity variations that are present on top of the large constant background. The ratio between the background and the signal increases with increasing objects' complexity. Scale-bars correspond to 7 speckle grains.

Another important aspect that affects the measured autocorrelation signal-to-noise ratio and is important to assure successful reconstruction is the ensemble averaging of the speckle autocorrelation. In the derivations of Equation 2 it was assumed that the autocorrelation is a narrow peak on top of a constant background. This is rigorously true only if the autocorrelation is averaged over an infinite number of speckle grains. In practice, the autocorrelation background would contain residual statistical speckle noise, which is inversely proportional to square root of the number of speckles captured in a camera frame. For the rigorous analysis of this noise term, we refer the reader to the works in stellar speckle interferometry^{4, 5}, and to ⁶. In case that the number of captured speckles is too small, one can capture another frame from a different position (or at a later time in the case of dynamic scattering samples) as we have performed in the experiment of Figure 2i.

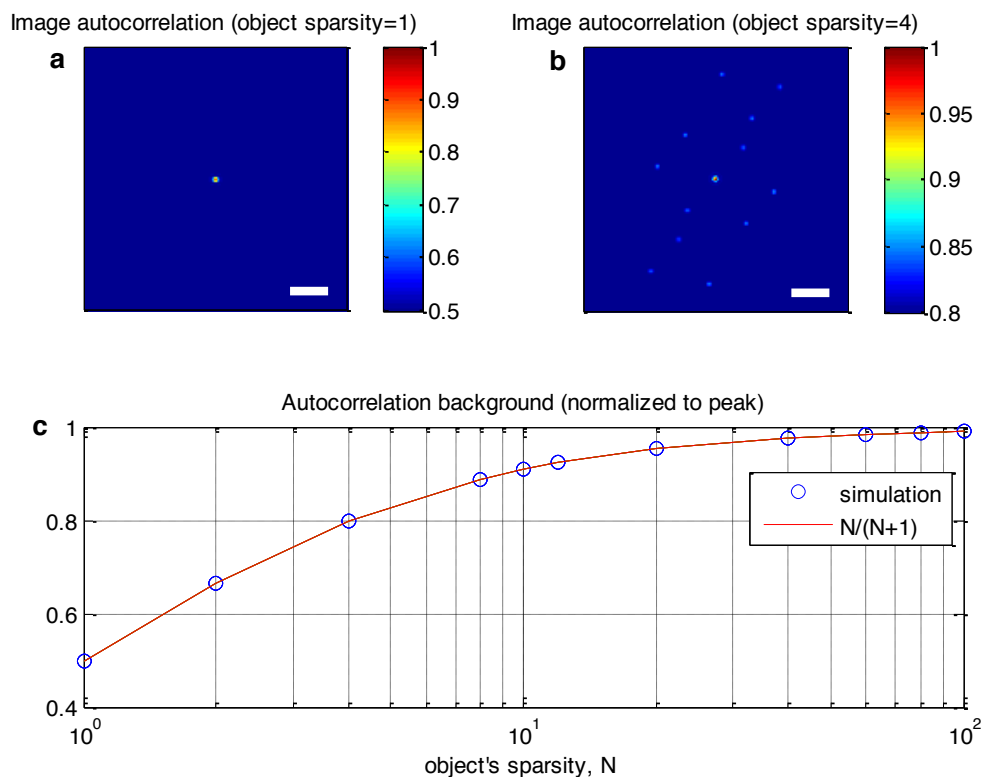
4. Analysis of the camera image autocorrelation background term as a function of the object's sparsity

In this section we analyze the magnitude of the constant background term of the camera image autocorrelation, C , presented in Equation 2. This background term originates from the 2:1 peak to background ratio of the speckle intensity autocorrelation. Therefore for a point like object, the autocorrelation would be that of the speckled PSF, having a background to peak ratio of 0.5 (Supplementary Figure 4a).

Consider now an object with a sparsity N , which is given by the ratio between the bright area of the object to the diffraction limited resolution cell area, $(u\delta\theta)^2$. For simplicity of the analysis we assume here an object that is composed of N equally bright spots of normalized intensity equal to one. The autocorrelation of this object pattern is composed of a bright central spot of intensity N , and $N(N-1)$ additional side peaks of intensity 1 (see e.g. Supplementary Figure 4b for an $N=4$ sparse object). According to Equation 2, the autocorrelation of the scattered-light camera-image of this object is given by convolving the object's autocorrelation with the speckle autocorrelation, which is composed of a central peak of normalized intensity 1 and a background term of intensity 0.5 (Supplementary Figure 4a). The result of this convolution would be an autocorrelation with a background term equal to: $b=0.5[N + N(N-1)]=0.5N^2$, and a central peak of intensity: $p = N+0.5N(N-1) = 0.5N^2+0.5N$. Thus, the background to peak ratio of the autocorrelation of the camera image would be:

$$b/p = N/(N+1).$$

In Supplementary Figure 4c we plot this calculated autocorrelation background-to-peak ratio as a function of the object sparsity, along with the result of numerical simulation performed for objects containing N randomly positioned bright resolution cells, showing the excellent correspondence of the above analysis.



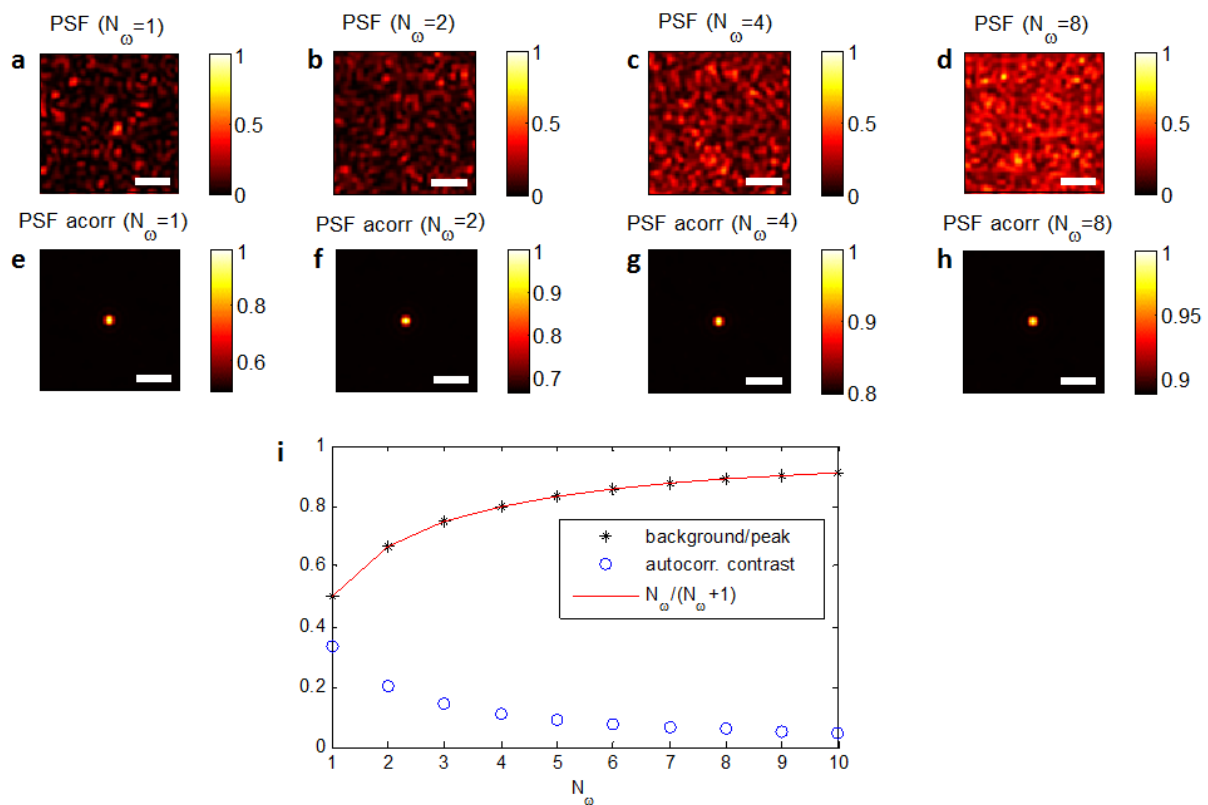
Supplementary Figure 4. Scattered light (camera image) autocorrelation background, C , as a function of the object's sparsity. **a**, Numerically simulated autocorrelation for an object composed of a single bright resolution cell, the background to peak ratio is equal to 0.5, as is the case for the intensity autocorrelation of a single speckle intensity pattern. **b**, same as (a) but for an object composed of $N=4$ (randomly positioned) bright resolution cells, i.e. an $N=4$ sparse object; the autocorrelation background is increased to 0.8 of the central autocorrelation peak value. **c**, numerically simulated (blue circles) and theoretically expected (red curve) values for the autocorrelation background-to-peak ratio as a function of the object sparsity, N . Scale-bars correspond to 10 speckle grains.

5. Effect of detected spectral bandwidth on the speckled PSF, $S(\theta)$, and its autocorrelation

As mentioned in the manuscript, one can in principle use a detection bandwidth larger than the speckle spectral decorrelation bandwidth, $\delta\omega$, and still be able to effectively employ the presented approach. As we show below, this would only lower the raw image contrast, but would not affect the imaging resolution, as the autocorrelation of $S(\theta)$ remains a sharply peaked function (see Supplementary Figure 5).

The reason for this is that in the case of a detection bandwidth $\Delta\omega$ that is N_ω times larger than the spectral decorrelation bandwidth: $\Delta\omega = N_\omega \delta\omega$, the raw camera image for a point-like object would be the intensity-sum of several uncorrelated speckle patterns, each having similar speckle grain size. Consequently, the system's PSF would still exhibit a diffraction limited autocorrelation peak, albeit with an increased background term (Supplementary Figure 5). Thus a broader spectral bandwidth is acceptable if one can compromise the contrast of the initial raw image (i.e. if one has sufficient camera dynamic range, full well depth, and signal-to-noise ratio).

To offer a verification of this fact, we have performed a set of numerical simulations where we have calculated the autocorrelation of a point-spread-function composed of an incoherent intensity-sum of a varying number of spectrally uncorrelated speckle patterns, N_ω . The results of these simulations appear in Supplementary Figure 5. As can be observed, the effect of increased detection bandwidth is only in an increase in the PSF autocorrelation background, and not in loss of resolution.



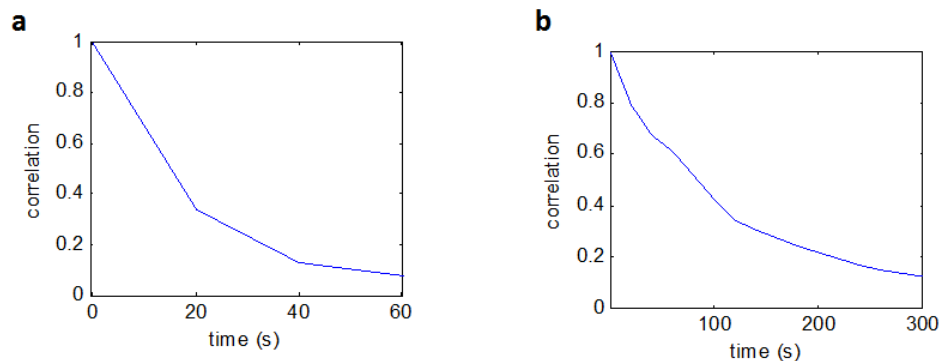
Supplementary Figure 5: **a-d**, Simulated PSF, $S(\theta)$, composed of the intensity sum of N_ω uncorrelated speckle patterns, as a function of the ratio $N_\omega = \Delta\omega / \delta\omega$, between the detection bandwidth $\Delta\omega$, and the speckle spectral decorrelation bandwidth, $\delta\omega$. Scale-bars correspond to 5 speckle grains; **e-h**, autocorrelation of the corresponding PSFs. The autocorrelation peak remains with a dimensions of a diffraction limited spot (a single speckle grain), but the autocorrelation background-to-peak ratio is reduced. **i**, autocorrelation background to peak ratio and contrast as a function of N_ω .

6. Scattering samples characterization

In this section we give the experimental characterization of various parameters of the scattering samples used in our experiments. These samples include a Thorlabs 220grit ground glass diffuser, a 0.3-0.5mm thick chicken breast tissue and a $\sim 80\mu\text{m}$ thick shallot skin.

6a. Speckle decorrelation time

The biological samples speckle decorrelation time was measured by illuminating the samples with a spatially coherent plane wave and calculating the correlation between the speckle intensity patterns measured over time by the sCMOS camera. The measured graphs for the two samples used ($\sim 300\mu\text{m}$ -thick chicken breast sample and thin shallot slice) are presented in Supplementary Figure 2.



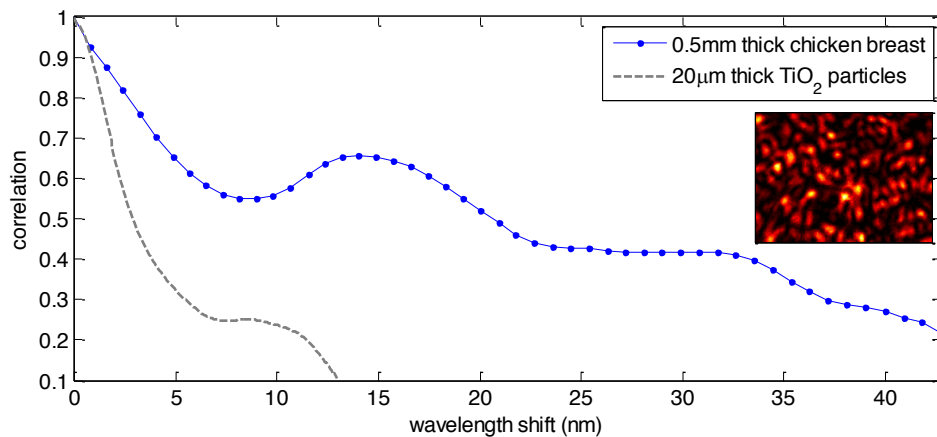
Supplementary Figure 6: Speckle decorrelation time for the biological scattering samples. **a**, $80\mu\text{m}$ -thick shallot skin, **b**, $\sim 300\mu\text{m}$ -thick chicken breast sample.

6b. Spectral decorrelation bandwidth characterization for $\sim 0.5\text{mm}$ thick chicken breast sample

We have characterized the speckle spectral decorrelation bandwidth of a $\sim 500\mu\text{m}$ -thick chicken breast sample. To this end, we have imaged the speckle pattern that is formed through the sample when the sample is illuminated by a narrowband tunable laser at different wavelength (Spectra-Physics Mai-Tai). The speckle spectral decorrelation width is quantified by calculating the intensity correlation between the speckle patterns at different wavelengths. The lasing wavelength was scanned between 765nm to 808nm in 50 steps.

The results of this measurements appear in Supplementary Figure 7. The speckle spectral decorrelation bandwidth has a value of $>10\text{nm}$, corresponding to a required coherence length of $<60\mu\text{m}$, of the order of 10% of the sample thickness. An expected result from such a forward-scattering sample⁷ having a thickness of the order of the transport mean free path. A curve of the spectral correlation width of a $20\mu\text{m}$ -thick sample of TiO_2 particles of diameter $<250\text{nm}$, measured with the same setup, is plotted as well for reference.

The transport mean free path of the ZnO sample used in the reflection experiments was characterized to be $2.1\mu\text{m} \pm 0.2\mu\text{m}$ at 748nm wavelength by Curry et al. [Optics Letters, 36, 17, 3332-3334 (2011)]. This value was used to calculate its spectral decorrelation bandwidth in the main text.



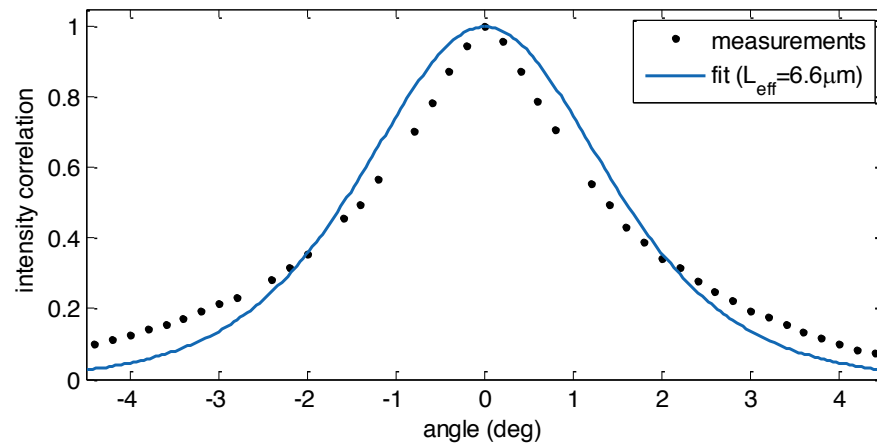
Supplementary Figure 7: Measurement of the spectral speckle decorrelation bandwidth. For a ~0.5mm-thick chicken breast sample (blue dots), and 20µm thick layer of TiO₂ particles of diameter <250nm (dashed gray). Inset: speckle pattern measured through the chicken breast sample at laser wavelength of 775nm.

The shallot sample temporal decorrelation time was, unfortunately, too short to enable us to characterize its spectral decorrelation bandwidth. However, considering its thickness, it may well be considered as a surface scattering (dynamically-varying) diffuser. Thus, similar to the ground glass diffuser used, its spectral decorrelation bandwidth will be dominated by geometrical path length differences^{8,9}.

6c. Memory-effect angular range (FOV limitation)

The memory effect angular range for a ~0.5mm thick chicken breast tissue was characterized by placing the sample on a rotation stage, illuminating it with a plane wave from a narrowband 532nm laser (8mm beam diameter), and plotting the intensity correlation of the measured speckle patterns imaged by a camera at a distance of 33cm on the other side of the sample, as a function of the sample rotation angle (Supplementary Figure 8). To take into account the additional spatial shift of the observed speckle pattern on the camera, which is observed in addition to the pattern decorrelation at each rotation angle, the central part of the speckle pattern was cross-correlated to a reference pattern taken at a fixed angle with various different added spatial shifts. The correlation value was taken as the maximal value for the cross-correlation term.

Interestingly, fitting the measured graph to the single-parameter theoretical memory effect curve in the diffusive regime: $C(\theta, L) = k_0 \theta L_{\text{eff}} / \sinh(k_0 \theta L_{\text{eff}})$, where $k_0 = 2\pi/\lambda$ [Feng et al. PRL 61, 7 (1988)], gives an effective sample thickness, L_{eff} of ~7µm, almost two orders of magnitude smaller than the physical thickness of the 0.5mm chicken breast sample. An encouraging result for employing the technique for imaging at similar depths. Note that the exact shape of the measured curve is somewhat different than the theoretical one due to the fact that the sample thickness is not considerably larger than its transport mean free path, as assumed in the theoretical derivation of Feng et al.¹⁰



Supplementary Figure 8: characterization of the memory effect angular range for a 0.5mm thick chicken breast tissue. The black dots are the measured speckle intensity correlation as a function of the sample rotation angle when illuminated by a plane wave beam with a diameter of 8mm. The speckle patterns are measured by a PCO edge 5.5 sCMOS camera. The blue curve is a fit to the theoretical expected correlation in the diffusive regime: $C(\theta, L) = k_0 \theta L_{\text{eff}} / \sinh(k_0 \theta L_{\text{eff}})$, where $k_0 = 2\pi/\lambda$ [Feng et al. PRL 61, 7 (1988)].

The 220grit ground glass diffuser (Thorlabs) memory effect range was characterized by Bertolotti et al.¹¹, and the transport mean free path of the FOV in reflection for the ZnO sample is given by its transport mean free path of $l^* = 2.2\mu\text{m}$ (as characterized by Curry et al.¹²) $\Delta\theta_{\text{FOV}} \approx \lambda / \pi l^* \approx 4.5^\circ$.

Unfortunately, the shallot skin sample too fast to measure its memory effect range.

7. Image retrieval algorithm (phase retrieval)

The object image is retrieved from its autocorrelation, which is calculated from the measured scattered light camera image. Given the processed (smoothened and envelope corrected) camera image $I(x,y)$ (see *Methods*), the scattered light autocorrelation, $R(x,y)$, is calculated by an inverse two-dimensional Fourier transform of its energy-spectrum:

$$R(x,y) = I(x,y) \star I(x,y) = FT^{-1}\{|FT\{I(x,y)\}|^2\}$$

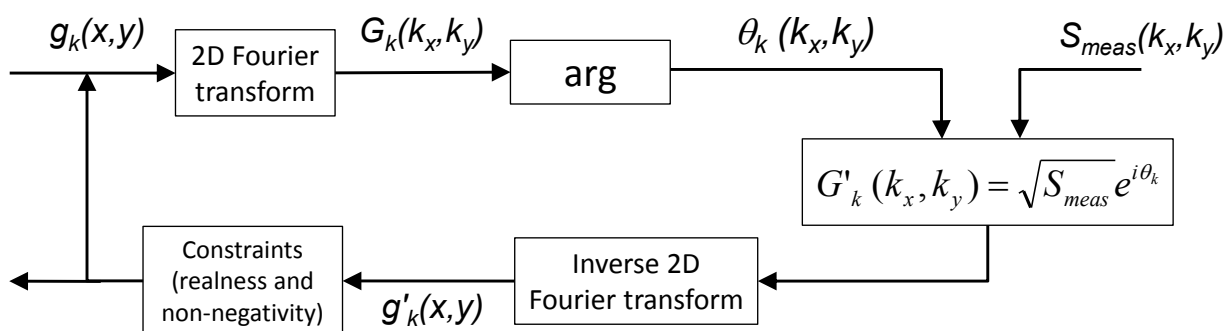
According to the Wiener–Khinchin theorem, the object’s power spectrum, $S_{meas}(k_x,k_y)$, is the Fourier transform amplitude of its autocorrelation. Therefore we calculate the object’s power spectrum by performing a 2D Fourier transform of the central part of this autocorrelation, after windowing with a windowing function $W(x,y)$ (which was either a rectangular or a Tukey window, see *Methods*):

$$S_{meas}(k_x,k_y) = |FT\{W(x,y)R(x,y)\}|$$

At this point, the ‘only’ missing information required to reconstruct the object’s image is the phase of its 2D Fourier transform, which is retrieved by an iterative Fienup-type phase-retrieval algorithm¹³. The phase-retrieval algorithm was implemented according to the recipe given by Bertolotti et al.¹¹. A block-diagram of this algorithm is given in Supplementary Figure 9. This modified Gerchberg-Saxton algorithm starts with an initial guess for the object pattern $g_1(x,y)$, chosen as a random pattern in our experiments. This initial guess is entered to the algorithm that performs the following four steps at its k^{th} iteration:

- 1) $G_k(k_x,k_y) = FT\{g_k(x,y)\}$
- 2) $\theta_k(k_x,k_y) = \arg\{G_k(k_x,k_y)\}$
- 3) $G'_k(k_x,k_y) = \sqrt{S_{meas}(k_x,k_y)}e^{i\theta_k(k_x,k_y)}$
- 4) $g'_k(x,y) = FT^{-1}\{G'_k(k_x,k_y)\}$

Where the measured information on the object’s autocorrelation is used in the third step.



Supplementary Figure 9: Block diagram of the iterative phase-retrieval algorithm used. The algorithm used is the Fienup’s HIO phase-retrieval algorithm¹³ that was implemented according to Bertolotti et al.¹¹, followed by Fienup’s error-reduction algorithm. Both algorithms are based on an iterative modified Gerchberg-Saxton algorithm whose block diagram is shown. $S_{meas}(k_x,k_y)$ is the Fourier transform amplitude of the experimentally measured autocorrelation. According to Equation 2 of the main text and the Wiener–Khinchin theorem $S_{meas}(k_x,k_y)$ is equal to the object’s image power spectrum $S_{meas}(k_x,k_y) = |F\{O(x,y)\}|^2$.

The input for the next ($k+1$) iteration, $g_{k+1}(x,y)$, is obtained from the output of the k^{th} iteration, $g'_k(x,y)$, by imposing physical constraints on the object image, it being real and non-negative in our implementation. Following Bertolotti et al.¹¹ we have used two types of implementations of these constraints into the algorithm, termed the ‘Hybrid Input-Output (HIO)’ and the ‘Error reduction’ algorithms, as pioneered by Fienup¹³. These algorithms are described by:

$$g_{k+1}(x,y) = \begin{cases} g'_k(x,y) & \text{for } (x,y) \notin \Gamma \\ 0 & \text{for } (x,y) \in \Gamma \end{cases}$$

For the Error-reduction algorithm.

And:

$$g_{k+1}(x,y) = \begin{cases} g'_k(x,y) & \text{for } (x,y) \notin \Gamma \\ g_k(x,y) - \beta g'_k(x,y) & \text{for } (x,y) \in \Gamma \end{cases}$$

For the HIO algorithm.

Where Γ is the set of all points (x,y) on $g'_k(x,y)$ that violate the physical constraints, and β is a feedback parameter that control the convergence properties of the algorithm.

Following Bertolotti et al.¹¹, first a few thousands iterations of the hybrid input-output (HIO) algorithm¹³ were ran with a decreasing beta factor from $\beta=2$ to $\beta=0$, in steps of 0.04. For each β value, 40 iterations of the algorithm were performed (i.e., a total of 2000 iterations). The result of the HIO algorithm was fed as an input to additional 40 iterations of the ‘error reduction’ algorithm to obtain the final result.

Importantly, to assure faithful reconstruction of each image, several different runs of the algorithm (from 20 up to 400, typically 50) were performed with different random initial conditions, and the reconstruction having the closest Fourier spectrum to the measured autocorrelation Fourier transform (lowest mean-square-error) was chosen as the final reconstructed result. We have noticed that for some of the objects (mostly the continuous ones, like the lettered objects of Figure 5) the reconstruction fidelity depended on the windowing function used.

References

1. Dowski, J.E.R. & Cathey, W.T. Extended depth of field through wave-front coding. *Applied optics* **34**, 1859-1866 (1995).
2. Cathey, W.T. & Dowski, E.R. New Paradigm for Imaging Systems. *Applied Optics* **41**, 6080-6092 (2002).
3. Goodman, J.W. Speckle phenomena in optics : theory and applications. (Roberts & Co., Englewood, Colo.; 2007).
4. Dainty, J.C. Laser speckle and related phenomena. (Springer, 1984).
5. Ayers, G., Northcott, M. & Dainty, J. Knox-Thompson and triple-correlation imaging through atmospheric turbulence. *JOSA A* **5**, 963-985 (1988).
6. Skipetrov, S.E. et al. Noise in laser speckle correlation and imaging techniques. *Optics Express* **18**, 14519-14534 (2010).
7. Cheong, W.-F., Prael, S.A. & Welch, A.J. A review of the optical properties of biological tissues. *IEEE journal of quantum electronics* **26**, 2166-2185 (1990).
8. Tal, E. & Silberberg, Y. Transformation from an ultrashort pulse to a spatiotemporal speckle by a thin scattering surface. *Opt Lett* **31**, 3529-3531 (2006).
9. Small, E., Katz, O. & Silberberg, Y. Spatiotemporal focusing through a thin scattering layer. *Optics Express* **20**, 5189-5195 (2012).
10. Feng, S., Kane, C., Lee, P.A. & Stone, A.D. Correlations and Fluctuations of Coherent Wave Transmission through Disordered Media. *Physical Review Letters* **61**, 834-837 (1988).
11. Bertolotti, J. et al. Non-invasive imaging through opaque scattering layers. *Nature* **491**, 232-234 (2012).
12. Curry, N. et al. Direct determination of diffusion properties of random media from speckle contrast. *Optics letters* **36**, 3332-3334 (2011).
13. Fienup, J.R. Phase retrieval algorithms: a comparison. *Applied optics* **21**, 2758-2769 (1982).